J. Fluid Mech. (2004), vol. 510, pp. 1–28. © 2004 Cambridge University Press
DOI: 10.1017/S0022112004009140 Printed in the United Kingdom

Proper orthogonal decomposition in the analysis of a laboratory simulation of land- and sea-breeze regimes

By ANTONIO CENEDESE AND PAOLO MONTI

Dipartimento di Idraulica Idraulica, Trasporti e Strade, Università degli Studi di Roma "La Sapienza",
Via Eudossiana 18, 00184 Roma, Italia
antonio.cenedese@uniroma1.it

(Received 10 September 2002 and in revised form 13 January 2004)

A land- and sea-breeze (LSB) circulation under a calm stably stratified environment was simulated in the laboratory using a temperature-controlled water tank. The floor of the tank was divided into two sections representing land and sea. Two heat exchangers, each of them connected to a thermostat, simulated the diurnal thermal cycle typically experienced by the surface in coastal zones. A third heat exchanger positioned at the top of the tank provided a stable thermal stratification. Particle-tracking velocimetry was applied to evaluate the two-dimensional velocity field in the vertical centreline section of the tank orthogonal to the coastline, while a rack of thermocouples measured the vertical temperature profile near the coastline and further inland. It is shown that the overall flow consists of a closed circulation caused by the periodic change of the horizontal temperature difference between land and sea surfaces. Furthermore, the formations of cellular convection during the first phase of warming of the land-side as well as the genesis of the sea-breeze front were detected and analysed. Application of the proper orthogonal decomposition (POD) technique allowed the vortical large-scale structures in the flow to be determined. The results suggest that the energy contained in the first POD eigenmodes rapidly converged with the first mode, associated with the overall LSB circulation, being dominant with 73% of the energy. The other less energetic modes were mainly associated with the cellular convection.

1. Introduction

Land- and sea-breeze (LSB) circulations are complex phenomena which affect the local meteorology of the atmosphere in proximity to the shoreline (see Simpson 1994 for a comprehensive review). These winds, caused by the different responses of land and water surfaces to the solar radiation on clear days, belong to the well-known class of flows called 'thermal circulation', and have typical horizontal scales of the order of 100 km or more. In fact, because of the large heat capacity and intense mixing of the ocean, the water surface maintains a nearly constant temperature during the diurnal cycle. On the other hand, the earth's surface warms and cools very rapidly, giving rise to a land–water temperature difference. Therefore, heating during the day makes the air above the land lighter with respect to the air above the water, and a horizontal pressure gradient forms, triggering a wind directed landward (sea-breeze) at low levels. An offshore wind (known as return or compensating flow) forms at the upper levels. At night, radiative cooling causes the land temperature to drop below that of the water, and the horizontal pressure gradient is inverted with respect to that observed in the daytime: the wind is directed offshore at low levels (land-breeze) and landward at high levels (return flow). In the absence of synoptic winds which can either strengthen or inhibit thermal circulations, sea-breeze currents are characterized by sustained wind speeds, usually 3–5 m s^{-1}, and by depth of the order of 300 m. Return flows typically show velocity and depth of the order of 1–2 m s^{-1} and 500–2000 m, respectively (Simpson 1994). LSBs are clear examples of gravity currents, that is, flow of heavy fluid under a lighter one. Field observations have shown that the head of these currents is generally of frontal type, accompanied by a steep variation in air temperature, humidity and wind direction (Chiba 1993; Helmis *et al.* 1987). The front is characterized by strong updrafts at the head and intense mixing with the surrounding fluid.

Evidence for LSB circulation is found all over the world. LSB circulation characterizes the climate of coastal regions and affects maritime activities in proximity to the shoreline. The action of LSBs can also influence the transport of pollens (Raynor, Hayes & Odgen 1974) and strongly affects the dispersion of atmospheric pollutants and their concentration at ground level (Simpson 1994). It is of note that if the coastal zone is characterized by complex topography (i.e. hills and mountains), other thermally induced winds such as mountain and valley breezes can strongly modify the characteristics of the LSB regimes.

A number of field campaigns and both analytical and numerical models developed in previous decades have clarified some of the major characteristics of the LSB regimes. Most of the surface-layer measurements have been carried out using classic sensors such as anemometers and thermometers, while remote sensors such as SODAR and LIDAR have allowed us to observe LSB circulations along a vertical profile up to heights of the order of 1 km (see Simpson 1994 and references therein). However, although field experiments represent the ‘truth’ by definition, they are very expensive and the results are generally limited to the particular case study.

The intrinsic limitations of full-scale experiments have induced many workers to find general analytical solutions for LSB regimes for idealized cases. The majority of the analytical models proposed in the past are based on the linear theory developed by Walsh (1974), in which the nonlinear term of the momentum equation is linearized about a basic current (i.e. geostrophic wind) perpendicular to the coastline (assumed as a straight line). Although the linear theory has proved to be a powerful tool in understanding important aspects of LSBs, it does not include many parameters which play important roles in the phenomena (i.e. diurnal variation of the land temperature, momentum and eddy diffusivities, prevailing winds, Coriolis parameter and atmospheric stability) as well as topographic effects. One of the consequences is that LSB circulation predicted by the linear theory is symmetric and frontogenesis cannot be modelled.

The acceleration of computational performance explains the recent massive employment of numerical meso-β scale (20–200 km) models for solving LSB flows. The majority of them are based on the k–ε closure assumption. It should be noted that numerical models have limitations (initial and boundary conditions, computer resources, grid resolution) and drawbacks. For example, parameterization of small-scale stratified turbulence remains a serious challenge (Pardyjak, Monti & Fernando 2002).

Laboratory simulations of LSBs have been conducted in water tanks in which a fluid flow results from the differential heating of the floor. The pioneers of this approach have been Kobayasi, Sasaki & Osanay (1937), who visualized both the streamlines and the inland sea-breeze front intrusion making use of fine aluminium powder as a tracer. Mitsumoto, Ueda & Ozoe (1983) improved on the previous experiment by employing a laser-Doppler system and a set of thermocouples to measure velocity and temperature, respectively. Experiments relevant to the dynamics of LSBs currents and frontogenesis were carried out by Linden & Simpson (1986) and Simpson & Linden (1989), among others.

Cenedese, Miozzi & Monti (2000) (hereinafter referred to as CMM) presented the preliminary results of a laboratory experiment performed to simulate LSB flows occurring in coastal zones during calm stably stratified conditions. The experimental apparatus used in CMM is shown in figure 1 (see next section for details). CMM found that a closed circulation (sea-breeze vortex) due to the horizontal temperature difference between land and sea was the main feature of the LSB, and that other structures formed and disappeared during the thermal cycle. In particular, they identified a phase of cellular convection over the land side during the first phase of warming (corresponding to the early morning hours in the atmosphere) followed by the landward intrusion of the sea-breeze current (as shown in the simple model of sea-breeze current in figure 2) and, finally, the establishment of the land-breeze resulting from the cooling of the land surface. An interfacial layer (also known as the 'zero-velocity layer') separated both the land- and sea-breeze currents from the elevated compensating flow. CMM observed that the foremost part, or nose, of the sea-breeze current was initially of a frontal type, characterized by large vertical velocity and strong mixing with the surrounding fluid. Owing to the convective activity associated to the inland well-mixed layer, the front progressively reduced its strength and then disappeared, in agreement with Linden & Simpson's (1986) experimental results. CMM also found that within the interfacial layer between the breeze and the return current, vortex-like structures existed, in particular after the passage of the sea-breeze front. A dynamic stability analysis of the flow, carried out calculating a suitable time-averaged gradient Richardson number $\overline{Ri_g} = \overline{N^2/(\mathrm{d}U/\mathrm{d}z)}$ along a vertical profile, showed that $\overline{Ri_g}$ within the interfacial layer was frequently below the critical value $Ri_{gc} = 0.25$. Here, $N = (g\alpha\Gamma)^{1/2}$ is the buoyancy (or Brunt–Väisälä) frequency, g the acceleration due to gravity, α the thermal expansion coefficient, $\Gamma = \partial T_a/\partial z$ the ambient lapse rate, U the streamwise velocity and z the vertical coordinate. Consequently, in agreement with the linear stability theory developed by Miles (1961) and Howard (1961), the vortical structures could be identified as Kelvin–Helmholtz billows, the primary mechanism for the vertical mixing between the sea-breeze flow and the compensating current as well as the observed deepening of the interfacial layer. The breakup of Kelvin–Helmholtz billows also generated wave perturbations in the wake of the front.

The presence of this variety of large structures which appear in the diurnal cycle (i.e. breeze vortex, cellular convection, sea-breeze front and Kelvin–Helmholtz billows) makes the application of proper orthogonal decomposition (POD) in analysing the laboratory LSB data very attractive, in that it permits the objective identification of large 'coherent structures' in the flow. Furthermore, transport and mixing of momentum and scalars are strongly dependent on the location and characteristics of these structures. In spite of this, a comprehensive discussion on this topic has not been yet made.

The POD analysis we will refer to in this work is based on the papers of Lumley (1967, 1981) and other subsequent works (see Berkooz, Holmes & Lumley 1993, hereinafter referred to as BHL, for a review of the POD technique; Holmes, Lumley & Berkooz 1996). It is generally recognized that the great advantage of using POD in

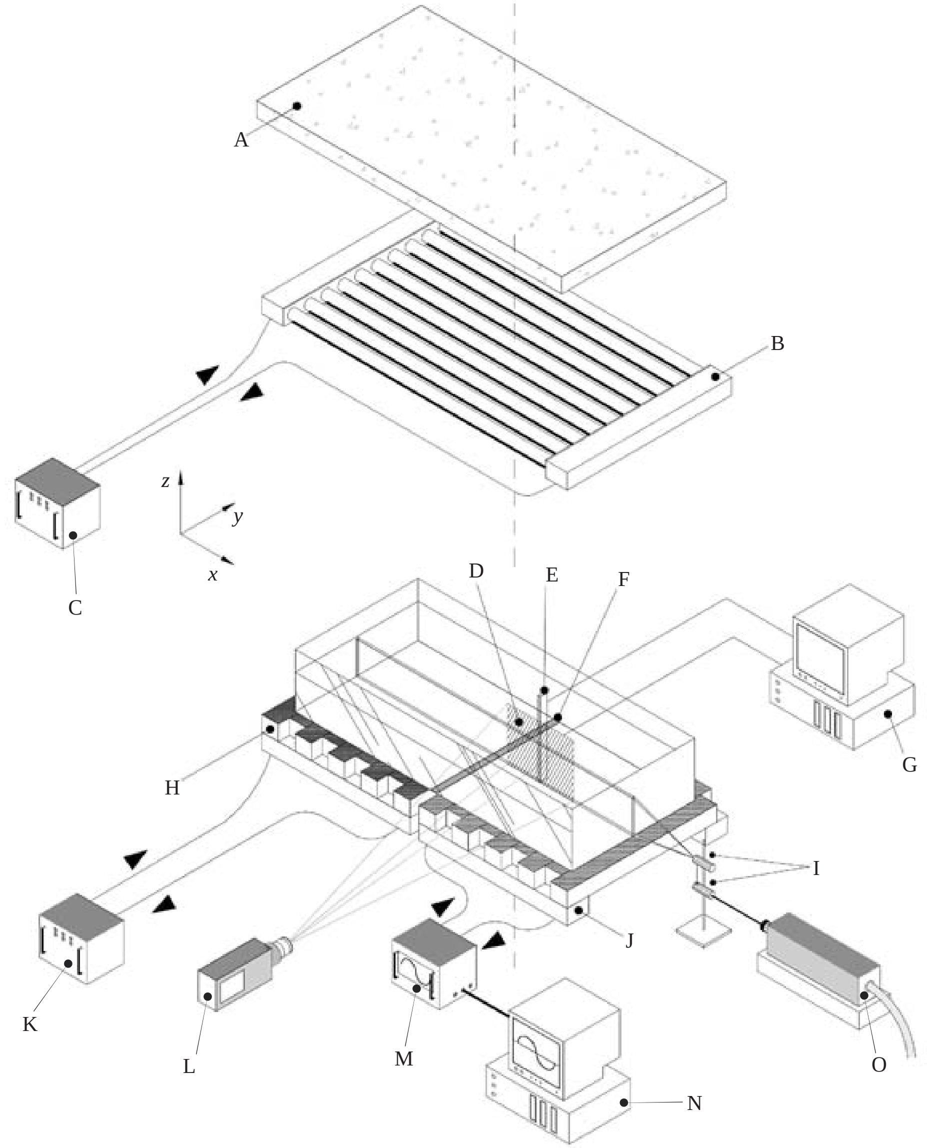

FIGURE 1. The experimental set-up: A, polystyrene sheet; B, heat exchanger (upper surface); C, thermostat (upper surface); D, framed area; E, thermocouple array; F, coastline; G, PC (thermocouples controller); H, heat exchanger (sea side); I, optics (mirrors, lens); J, heat exchanger (land side); K, thermostat (land side); L, video camera; M, thermocryostat (land side); N, PC (land temperature controller); O, laser.

turbulent flow analysis is its ability to recognise spatial and temporal coherent structures characterizing the flow field. The fundamental feature of POD is that it allows us to find an orthogonal set of vectorial deterministic spatial functions (i.e. eigenmodes) that represents the best approximation of the original set of the velocity field. The set of eigenmodes is the best in an energetic sense in that, among all the possible decompositions, it is the most efficient, i.e. the projection on the subspace will contain the most kinetic energy possible in an average sense. It should be noted

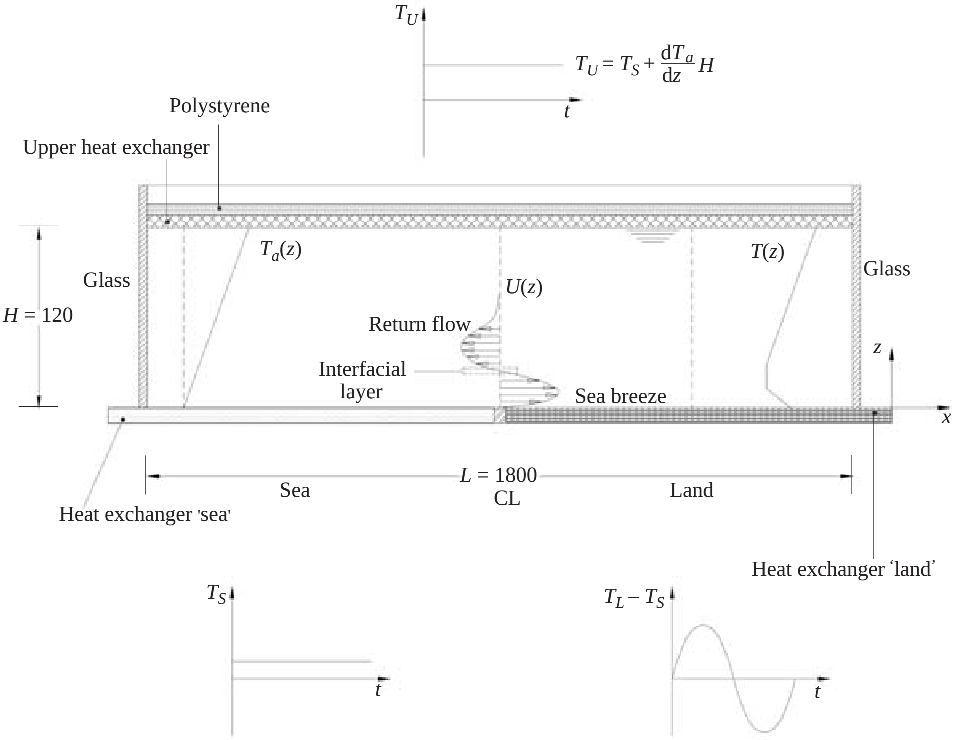

FIGURE 2. Diagram of the sea-breeze current. All measurements in mm.

that, in some cases, low-energy events could drive flow dynamics, especially if the system is near an instability. Moreover, as noted by Lumley (1981), POD modes are not always related to the underlying coherent structures.

Fisher *et al.* (1996) and Miozzi & Querzoli (1996) showed that experimental approaches such as particle image velocimetry (PIV) and particle tracking velocimetry (PTV) are particularly well suited to providing the set of instantaneous velocity fields required by POD. In fact, both methods give time varying Eulerian flow patterns on a regular grid. Consequently, the evaluation of the principal basis for each grid node as well as the time behaviour of the eigenvalues is possible. It should be noted that thermally-induced turbulent flows are characterized by infinite-dimensional phase space but, owing to their dissipative characteristics, such flows can be bounded into relatively low dimensional attractors (see, for example, Sirovich 1987).

From a theoretical point of view, POD theory asserts that the kinetic energy of the flow is spread over an infinite number of orthonormal eigenmodes. Therefore, in order to express the original instantaneous vector field, the whole set of eigenmodes should be employed. Nevertheless, a number of applications of POD have demonstrated that most of the kinetic energy is retained in the first 3–4 modes, for certain flows. For example, the analysis conducted by Glauser & George (1989) for a high-Reynolds number axisymmetric jet shear layer showed that the first three eigenmodes contained nearly 80% of the total kinetic energy of the flow. Similar results were found by Delville *et al.* (1999) in their investigation of coherent structures in a planar mixing layer and by Miozzi & Querzoli (1996) in a quasi two-dimensional convective flow. From a general point of view, this means that it is possible to recover the instantaneous shape of the flow structures making use of a low number of POD modes.

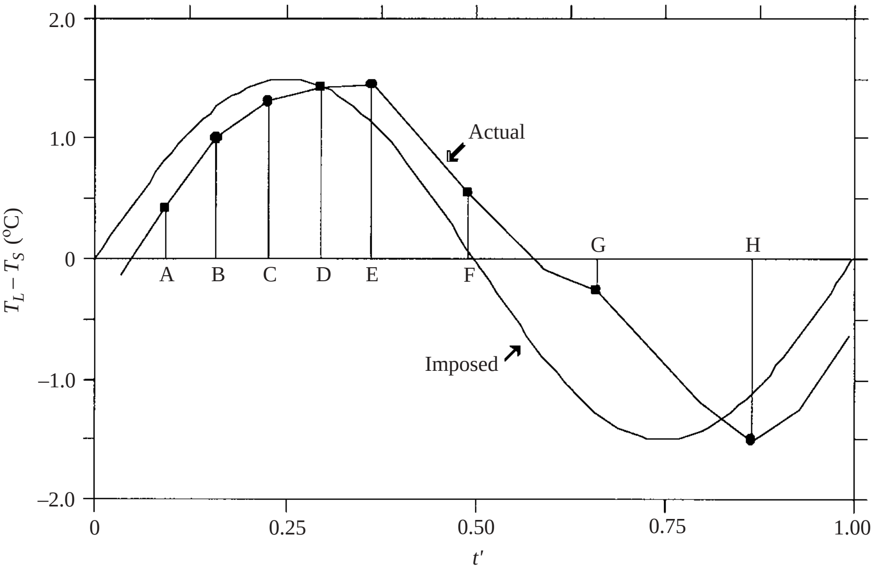

FIGURE 3. Thermal cycle expressed in terms of temperature differences between land and sea side (dashed and solid lines refer to the imposed and the actual T_L experienced by the land side, respectively). Lettered points correspond to the times referred to in the text: A, $t' = 0.091$; B, 0.159; C, 0.227; D, 0.295; E, 0.364; F, 0.492; G, 0.659; H, $t' = 0.864$.

The aim of this study is two-fold: first, to simulate in the laboratory the LSB regimes under a calm stably stratified environment, and secondly to investigate the characteristics of the large-scale structures in the flow by using the POD technique. Section 2.1 deals with the acquisition of the experimental data carried out by using the same facility and techniques as used by CMM, and basic elements of POD theory are given in § 2.2. Section 3.1 describes the data analysis in terms of average temperature and velocity fields taken during the various phases of the LSB regime. Section 3.2.1 describes the extraction and analysis of the POD eigenmodes obtained starting from the 'original' set of mean velocity fields calculated in § 3.1. Finally, § 3.2.2 outlines the velocity field recovery procedure used to obtain an objective measure of the weight that each mode has on the flow field. Summary and final discussion are given in § 4.

2. Procedure

2.1. *Experimental set-up*

The experiments were carried out in a rectangular tank (figures 1 and 2) filled with water with length $L = 1800$ mm, height $H = 200$ mm and a width of 600 mm (along the x-, z- and y-axis, respectively), open at the top and with an aluminium horizontal surface at the bottom. In order to allow for the visual observation of the flow, the lateral sides of the tank were made up of 10 mm thick transparent glass. The bottom was divided into two sections: land and sea sides. The latter was kept at a constant temperature $T_S = 26\,°\mathrm{C}$ throughout the experiment by means of a heat exchanger, connected to a thermostat, consisting of counter-flow channels. To simulate the diurnal changes of the land side temperature, T_L, a thermocryostat with microprocessor controller supplied a second heat exchanger. In doing so, T_L could vary sinusoidally around T_S (dashed line in figure 3). The time period and amplitude of the thermal cycle were set to $t_C = 2640\,\mathrm{s}$ and $T_C = 1.5\,^\circ\mathrm{C}$, respectively. The non-dimensional quantity $t' = t/t_C$ bounded in the range $0 \leqslant t' \leqslant 1$ was used as a non-dimensional time variable. Notice that owing to the thermal inertia of the system 'thermocryostat-pipes-heat exchanger' the actual thermal cycle of the land side (solid line in figure 3) undergoes a non-dimensional time delay of the order of 0.1 with respect to that imposed by the thermocryostat. The separation region between the land and sea side represented the coastline (hereinafter referred to as CL; the sea side and the land side are on the left-hand and right-hand sides of the CL, respectively). In order to restrict the vertical extension of the flow from the entire depth of the tank, the fluid was linearly stably stratified keeping the temperature of the free surface at the constant value $T_U = 38\,^\circ\mathrm{C}$ by using a third heat exchanger. Given the 120 mm depth of the water (see figure 2), the imposed vertical gradient of the ambient temperature was $\partial T_a/\partial z = 0.1\,^\circ\mathrm{C\,mm^{-1}}$. The corresponding Brunt–Väisälä frequency was $N \cong 0.5\,\mathrm{s^{-1}}$. A polystyrene sheet was placed over the top of the tank to reduce heat losses. The temperature of the sidewalls was not controlled, but it can be reasonably considered constant throughout the experiment. In order to obtain periodical conditions, several temperature cycles were imposed before the beginning of the measurements.

The PTV technique was applied to evaluate the velocity field in the centre of the tank along the (x, z)-plane orthogonal to the CL (see figure 1). A thin laser light sheet from a 3 W argon laser beam passing through an optical device illuminated the measurement plane. The water was seeded with pine pollen particles ($\sim 80\,\mu\mathrm{m}$ in diameter) which were assumed to be passively transported by the flow. A set of images was taken in a rectangular region in the proximity of the CL by means of a CCD video camera at 25 Hz. One out of every eight frames was automatically retrieved by using an animation controller, lowering the resulting sampling rate to 3.12 Hz. The framed area was 270 mm long (x-axis) and 120 mm high (z-axis). Hereinafter, we will refer to the left-hand bottom corner of the framed area as the origin of the x-axis. In doing so, the abscissa of the CL is at $x_{CL} = 30\,\mathrm{mm}$. After the experiment, each frame was digitized by a frame grabber with 752×576 pixel resolution and 256 grey levels. Particles were recognized on each digitized frame and the locations of the particles' centroids were computed and stored (about 3000 particles per frame were recorded on the investigated area). From the trajectories evaluated at each time instant from the positions of the centroids, the instantaneous Lagrangian velocity field was obtained by using two sequential (in time) frames and differencing. A (spatial) Gaussian interpolation algorithm was applied to the velocity samples in order to obtain a two-dimensional Eulerian description of the motion at a rate of 3.12 Hz on a 40×30 regular grid along the x- and z-axis.

Temperatures were acquired by means of ten T-type (copper–constantan) thermocouples placed on a vertical rake at a sampling rate of 1 Hz. In order to avoid, as far as possible, disturbances in the velocity field and light reflections, the temperature probes were positioned approximately 1 mm behind the measurement plane, equally spaced every 4 mm in the vertical from 0 to 36 mm. Several mean temperature profiles were carried out at CL ($x = x_{CL} = 30\,\mathrm{mm}$) and further inland ($x = x_{IN} = 120\,\mathrm{mm}$). Given a depth of flow of $\sim 50\,\mathrm{mm}$ (cf. § 3.1), the aspect ratio (height to width) of the test fluid region was $\sim 1/12$, sufficiently small to keep the flow two-dimensional. In fact, the results were shown to be insensitive to the location of the measurement plane if it was kept within a certain spatial range centred on $y = 0$. This is corroborated by the experiments conducted in similar conditions by Mitsumoto *et al.* (1983). It should also be mentioned that a consequence of the heat input to the water is that the heating and the induced circulation gradually eroded the imposed thermal stratification. However, according to our measurements, the stirring of the vertical thermal gradient above $z = 20$ mm was nearly negligible and the height of the induced circulation did not change appreciably from cycle to cycle. This can be explained by considering that the heat input was not continuous in time, but alternated with cooling.

2.2. *Calculation of the POD modes*

In this subsection, the basis of the POD technique in the context of vector fields will be briefly reviewed. An extended discussion on POD theory can be found in BHL.

Starting from an ensemble of realizations of the vector field $\boldsymbol{u}(\boldsymbol{x}, t)$, the problem is to find the deterministic function that is the most similar to the elements of $\boldsymbol{u}(\boldsymbol{x}, t)$ on average, where $\boldsymbol{x}$ is the position vector. In the remainder of this paper, it will be assumed that the ensemble $\boldsymbol{u}(\boldsymbol{x}, t)$ is square-integrable on a suitable finite domain S. The performance of an approximation of $\boldsymbol{u}(\boldsymbol{x}, t)$ can be expressed as:

$$\langle(\boldsymbol{u}(\boldsymbol{x}, t), \psi(\boldsymbol{x}))^2\rangle / (\psi(\boldsymbol{x}), \psi(\boldsymbol{x})), \tag{2.1}$$

where higher values mean better performance. In (2.1), the angle bracket, indicate the time average, $(\cdot,\cdot)$ the inner product between two suitable vector fields: $(\boldsymbol{f}(\boldsymbol{x}), \boldsymbol{g}(\boldsymbol{x})) = \int_S \boldsymbol{f}(\boldsymbol{x}) \cdot \boldsymbol{b}(\boldsymbol{x}) \cdot \mathrm{d}\boldsymbol{x}$ and $\Psi(\boldsymbol{x})$ defined in the next paragraph.

Equation (2.1) represents a classical problem in the framework of calculus of variations in that we are looking for a set of time-independent vector fields $\{\Psi_k(\boldsymbol{x})\} \equiv \Psi(\boldsymbol{x})$ such that its normalized inner product with $\boldsymbol{u}(\boldsymbol{x}, t)$ is a maximum, i.e. the projection process maximizes the energy contained in $\Psi(\boldsymbol{x})$ (note that k assumes the meaning of a member of the sequence and not of a vector component). In other words, the set $\Psi(\boldsymbol{x})$ is the most nearly parallel to $\boldsymbol{u}(\boldsymbol{x}, t)$ in an average sense and it is usually referred to as the set of coherent structures or modes. It can be shown that the problem of maximizing (2.1) corresponds to solving:

$$\int_S \boldsymbol{R}(\boldsymbol{x}, \boldsymbol{x}') \cdot \Psi(\boldsymbol{x}') \cdot \mathrm{d}\boldsymbol{x}' = \lambda \Psi(\boldsymbol{x}), \tag{2.2}$$

where $\Psi(\boldsymbol{x})$ is a set of eigenvectors, $\{\lambda_k\} \equiv \lambda$ is a set of eigenvalues and $R_{ij}(\boldsymbol{x}, \boldsymbol{x}') = \langle u_i(\boldsymbol{x}, t) u_j(\boldsymbol{x}', t)\rangle$ the two-point auto-correlation function.

Owing to the symmetry and the non-negative definitiness of the matrix $\boldsymbol{R}$, the spectral theorem assures both that the set of the eigenvalues is strictly positive and that the eigenvectors are mutually orthogonal. It can be shown (BHL) that each member of the ensemble of the vector fields $\boldsymbol{u}(\boldsymbol{x}, t)$ can be reconstructed via the so-called modal decompositions in the eigenmodes:

$$\boldsymbol{u}(\boldsymbol{x}, t) = \sum_k \xi_k(t) \psi_k(\boldsymbol{x}), \tag{2.3}$$

where the modal coefficients $\xi_k(t)$ are uncorrelated:

$$\langle \xi_i(t) \xi_j^*(t)\rangle = \delta_{ij} \lambda_i. \tag{2.4}$$

Here, the asterisk indicates the complex conjugation and δ_{ij} is the Kronecker delta. In this context, the set $\Psi(\boldsymbol{x})$ assumes the meaning of an empirical basis. It can be shown that the kth eigenvalue represents the average kinetic energy per unit mass in the kth mode and the time spent by the system along the kth eigenvector. Accordingly,

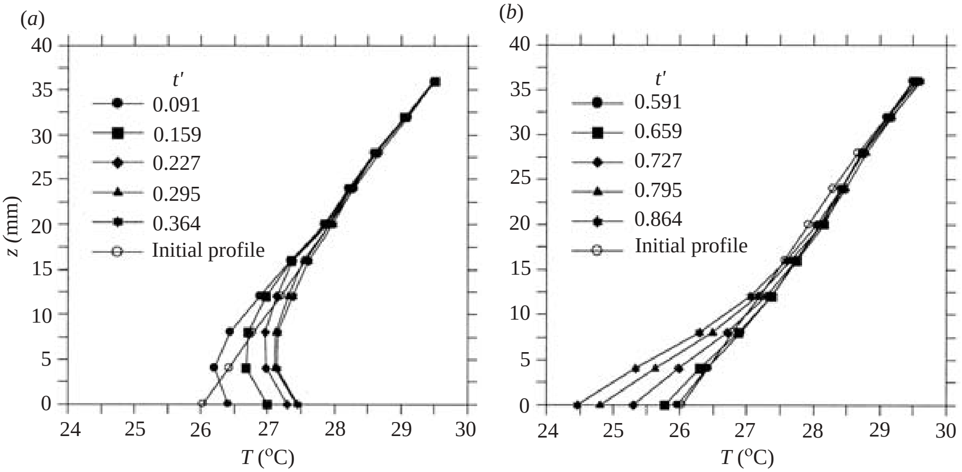

FIGURE 4. Mean temperature profiles measured at various times in the thermal cycle (cf. figure 3) at $x = x_{IN}$ when (*a*) $T_s < T_L$ and (*b*) $T_S > T_L$.

the energy of the flow can be defined as:

$$E(t) = \int_S [\boldsymbol{u}(\boldsymbol{x}', t)]^2 \cdot \mathrm{d}\boldsymbol{x}' = \sum_k \xi_k(t)^2. \tag{2.5}$$

In the analysis proposed in this paper, the procedure will be broken into three steps:

(i) evaluation of the two-point correlation matrix $R_{ij}(\boldsymbol{x}, \boldsymbol{x}') = \langle u_i(\boldsymbol{x}, t) u_j(\boldsymbol{x}', t)\rangle$ performed in time on the ensemble of the original vector fields $\boldsymbol{u}(\boldsymbol{x}, t)$;

(ii) solving the integral equation (2.2) to extract the set of eigenvalues $\{\lambda_k\}$ and the set of eigenvectors $\{\Psi_k(\boldsymbol{x})\}$;

(iii) evaluation of the instantaneous modal coefficients $\xi_k(t) = \psi_k(\boldsymbol{x}) \cdot \boldsymbol{u}(\boldsymbol{x}, t)$ determined by the projection of $\boldsymbol{u}(\boldsymbol{x}, t)$ on the solution $\{\Psi_k(\boldsymbol{x})\}$ of equation (2.2).

3. Results

3.1. *The temperature and velocity fields*

In this section, mean temperature vertical profiles and mean velocity patterns calculated during the principal phases of the phenomenon, that is, cellular convection, sea-breeze front genesis and its inland penetration, and both sea- and land-breeze regimes, will be discussed. Since the processes of interest are mainly related to large-scale structures (which have time scales of the order of minutes or more; CMM), an averaging time interval of $\Delta t = 10$ s (corresponding to ∼5 min in the real case) was selected. This yields 264 mean velocity and temperature fields in the thermal cycle. Averaging time intervals ranging from 20 to 50 s gave very similar statistics (not shown) suggesting that, because of the slowness of the phenomenon, during the chosen $\Delta t = 10$ s, the mean flow can be considered in a quasi steady-state.

Figure 4 shows the mean temperature profiles measured at x_{IN} in the vertical range $0 < z < 36$ mm for various points in time in the thermal cycle. The instant $t' = 0$ corresponds to the beginning of the thermal cycle, i.e. when T_L overcomes T_S, while the initial profile indicates the ambient stratification T_a imposed before the start of the cycle (figure 2). Examples of velocity fields taken in the vertical at the centre of

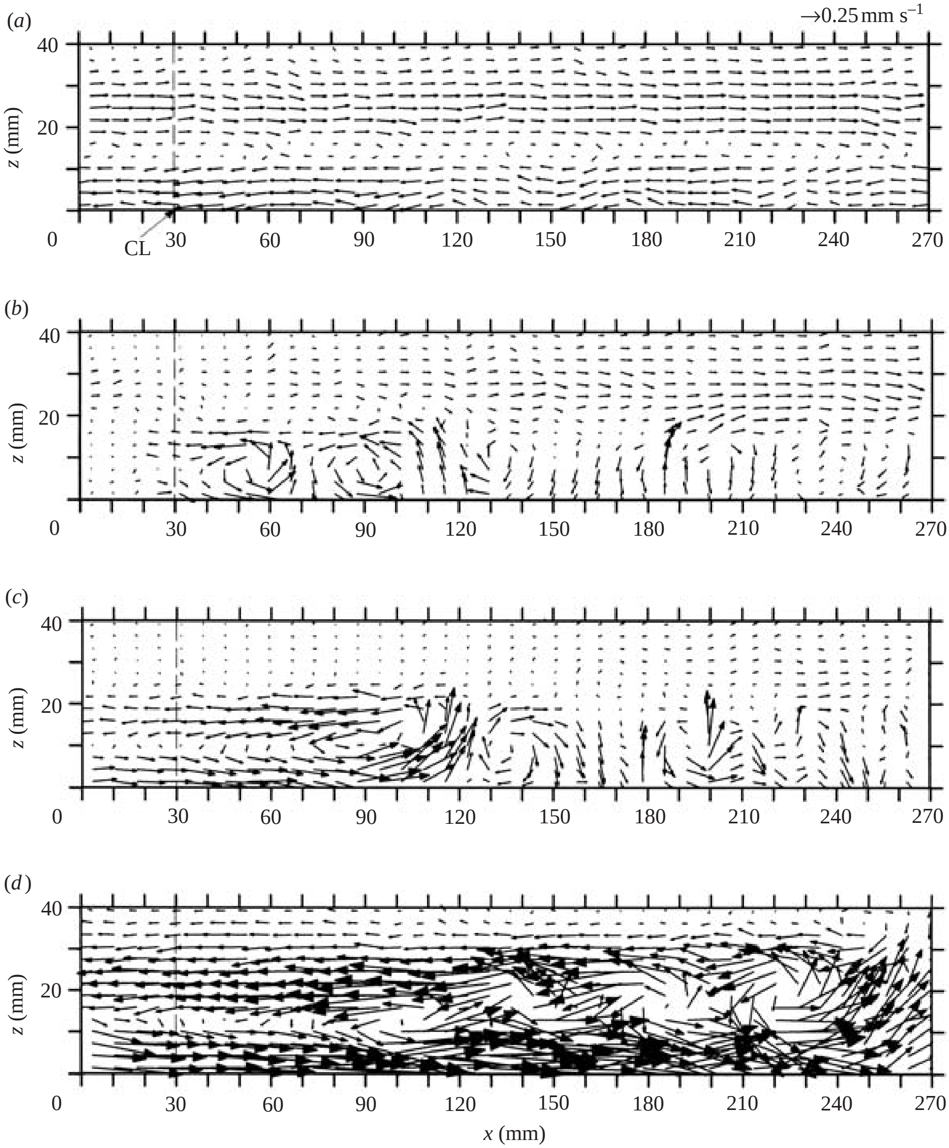

FIGURE 5(*a*–*d*). For caption see facing page.

the tank are depicted in figure 5 (the sea side is on the left-hand side of the CL and the land side is located on the right). Horizontal and vertical velocity profiles carried out at $x = x_{CL}$ and $x = x_{IN}$ are shown in figure 6(*a*–*d*) (upward vertical velocity W and landward (along the x-axis) velocity U are positive). Figure 5(*a*) shows the velocity field during the end of the land-breeze phase ($t' = 0.091$). The flow was seaward (from right to left) in the layer $0 < z < 10$ mm and landward (from left to right) at the upper levels ($z > 20$ mm). A clearly defined interfacial region separated the two layers (zero-velocity layer). At the same time, within $0 < z < 4$ mm, the fluid temperature rapidly increased as $z \rightarrow 0$ (figure 4*a*), as a result of the heating coming from the bottom. Notice the presence of the land breeze, even though the land temperature exceeded the sea temperature. This situation is typically observed in the real world during early

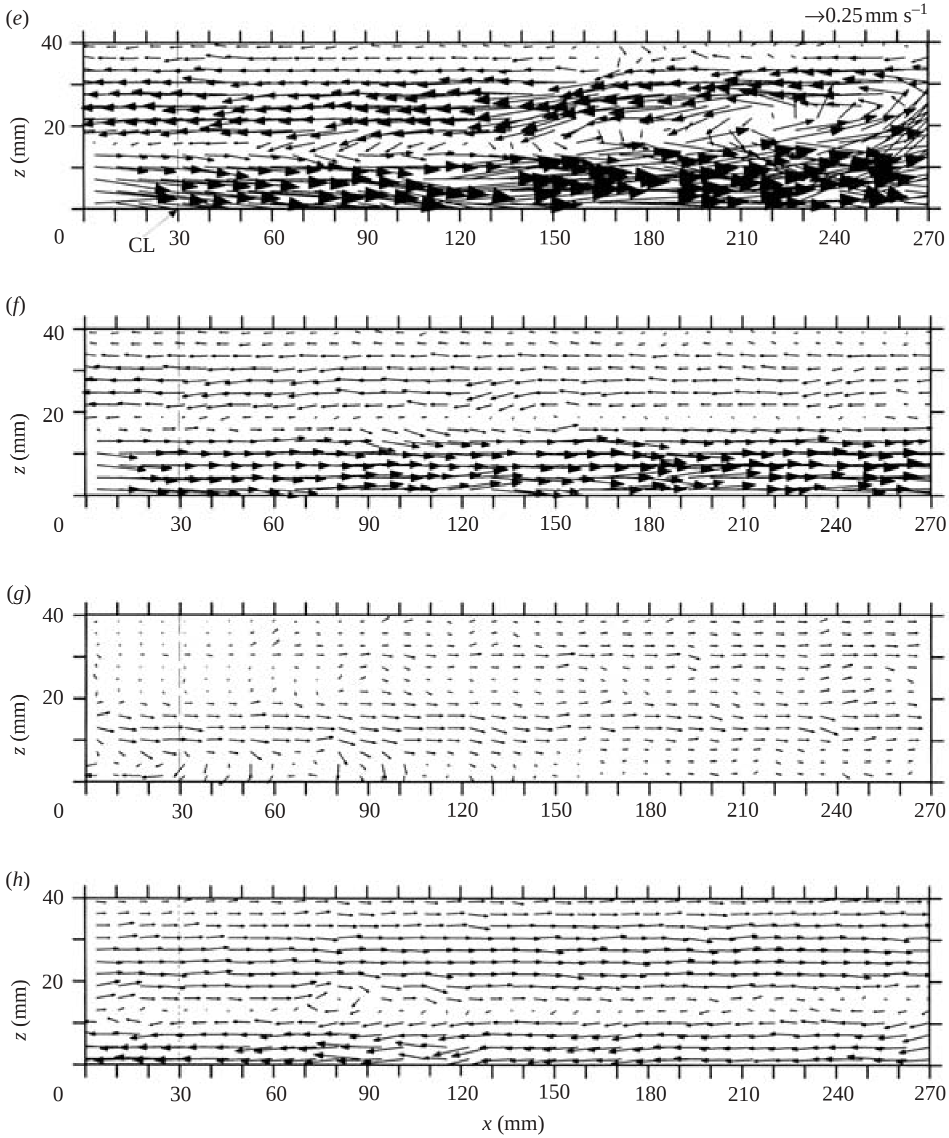

FIGURE 5. Mean velocity vectors measured during sequential phases of the thermal cycle (cf. figure 3); (*a*) residual land-breeze ($t' = 0.091$); (*b*) cellular convection ($t' = 0.159$); (*c*) sea-breeze onset and front formation ($t' = 0.227$); (*d*) sea-breeze intrusion and front strengthening ($t' = 0.295$); (*e*) sea-breeze ($t' = 0.367$); (*f*) sea-breeze weakening ($t' = 0.492$); (*g*) transition between sea- and land-breeze ($t' = 0.659$); (*h*) land-breeze ($t' = 0.864$).

morning when an offshore wind continues to flow, owing to the inertia, against the pressure gradient. Signatures of the two layers are also evident from the time history of U taken at x_{IN} within the land breeze ($z = 7$ mm), the return flow ($z = 22$ mm) and further above ($z = 57$ mm), where the fluid was nearly at rest (figure 7*a*).

The increasing supply of heat from the bottom surface was the trigger for the cellular convection clearly visible inland in figure 5(*b*) ($t' = 0.159$). In particular, the flow above the land side was characterized by a series of thermal updrafts and large regions of downdraft. In fact, when a stable and stratified fluid is heated from below,

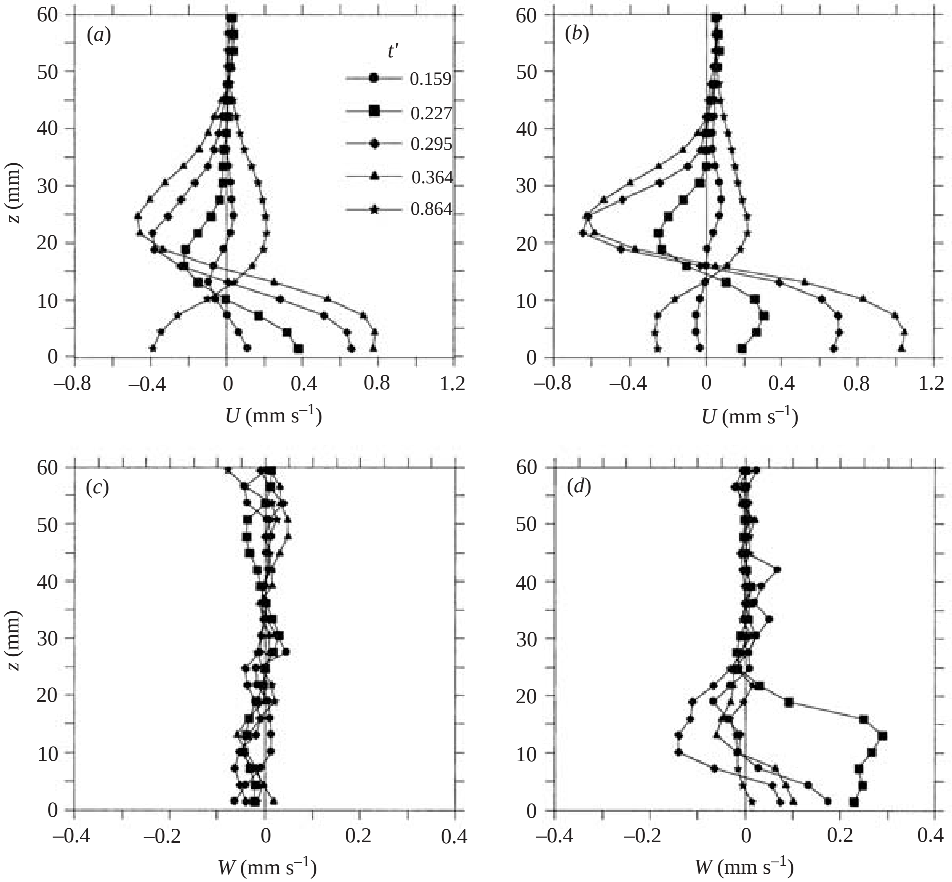

FIGURE 6. (*a*) Horizontal velocity profiles at $x = x_{CL}$; (*b*) horizontal velocity profiles at $x = x_{IN}$; (*c*) vertical velocity profiles at $x = x_{CL}$; (*d*) vertical velocity profiles at $x = x_{IN}$.

instability produces a Bénard-type cellular convection (Koschmieder 1993). As already evidenced experimentally (Deardorff & Willis 1985; Cenedese & Querzoli 1994) and numerically (see for example Moeng 1984), these thermal plumes, responsible for intense vertical mixing, look like thermals present over a land surface experiencing strong solar radiation. Figure 7(*b*), where the time histories of U and W measured at ($x_{IN}, z = 7$ mm) are shown, illustrates that the convection phase took place at x_{IN} during the time interval $0.125 < t' < 0.225$, i.e. when U was nearly zero and W assumed high positive values. Moreover, given the measured temperature vertical profiles, the bottom layer is recognized to be superadiabatic, while the overlaying layer showed the typical characteristics of a well-mixed layer (figure 4*a*). Also, the contour plot of the mean turbulent kinetic energy $TKE = (\overline{u'^2} + \overline{w'^2})/2$ calculated at $t' = 0.159$ (figure 8*a*) suggests that high levels of turbulence accompanied the convective cells. Here, $\overline{u'^2}$ and $\overline{w'^2}$ indicate the mean variance of the horizontal and the vertical velocity component, respectively.

Figure 5(*c*) gives an example of the velocity field observed when the sea breeze intruded inland bringing down the activity of the thermal plumes ($t' = 0.227$), in agreement with the numerical runs performed by Sha, Kawamura & Ueda (1991). Sha *et al.* (1991) also noted that, with the exclusion of the surface layer, within the

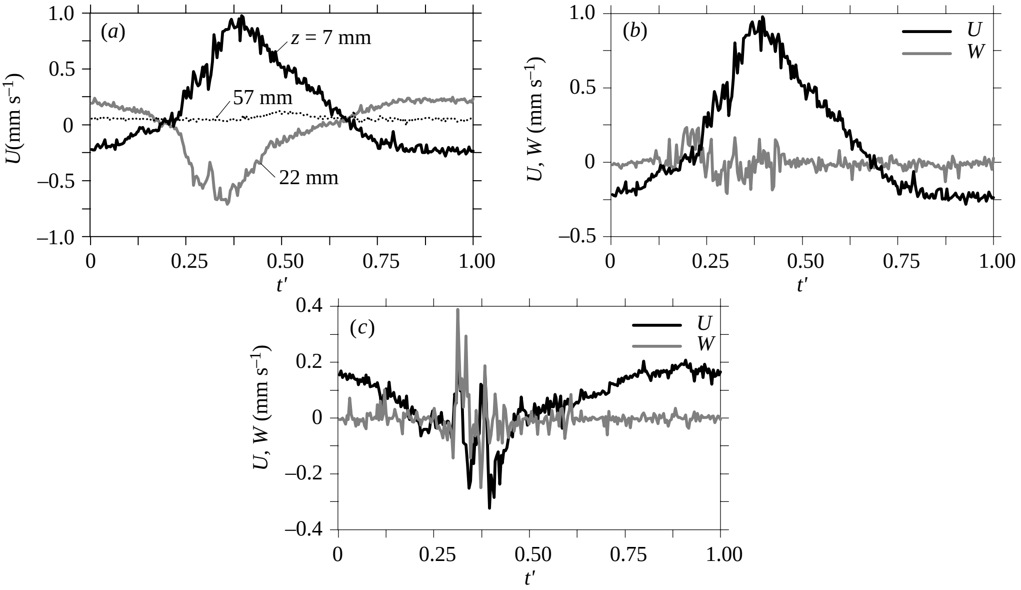

FIGURE 7. (*a*) Time history of the horizontal velocity component U taken at x_{IN} during the thermal cycle for various heights from the bottom. (*b*) as in (*a*) but for both the velocity components U and W at $(x_{IN}, z = 7\,\mathrm{mm})$. (*c*) as in (*b*), but within the interfacial layer ($x = 180\,\mathrm{mm}$, $z = 19\,\mathrm{mm}$).

sea breeze, the mean temperature profiles were approximately constant with height. The same behaviour was observed in our experiment (see profiles $t' = 0.227$, 0.295 and 0.364 shown in figure 4*a*). Both the decrement of the boundary-layer height detected in the wake of the sea-breeze current as compared with that observed during the phase of cellular convection (figure 5*b*) and the trend of the temperature profiles lead to the hypothesis that the boundary layer is in a state of forced convection, i.e. near neutral stability condition.

Meanwhile, a return flow directed offshore took place above the sea-breeze current, while in the portion of the land side where the sea-breeze current had not yet passed, the boundary layer was in a state of free convection. The compensating flow had been first observed at full-scale by means of pilot balloons (Koschmieder 1936). Also, numerical models have demonstrated the presence of the return flow as well as the zero-velocity layer (see for example Sha *et al.* 1991). However, it should be mentioned that their occurrence in the atmosphere is not always verified. One possible reason is the presence of synoptic winds that, even if weak, can dramatically change the structure of the elevated layers. Figure 5(*c*) also shows that a frontal-type raised head formed at the leading edge of the sea breeze current ($x \cong 120\,\mathrm{mm}$). A comparison between figures 6(*a*) and 6(*b*) reveals (cf. the lines with full squares) that the front grew owing to the greater velocity of the current behind the head with respect to the speed of penetration of the front. Notice that the shape of the front is similar to that typically observed at the leading edge of gravity currents (see Simpson 1994). Also, the front height is nearly twice the depth of the following sea breeze, in good agreement with the numerical simulations performed by Sha *et al.* (1991) and with the laboratory experiments reported by Simpson & Britter (1980). The front is accompanied by a strong vertical velocity (upward velocity peaks of $0.3\,\mathrm{mm\,s^{-1}}$ were measured, approximately one-third of the maximum horizontal

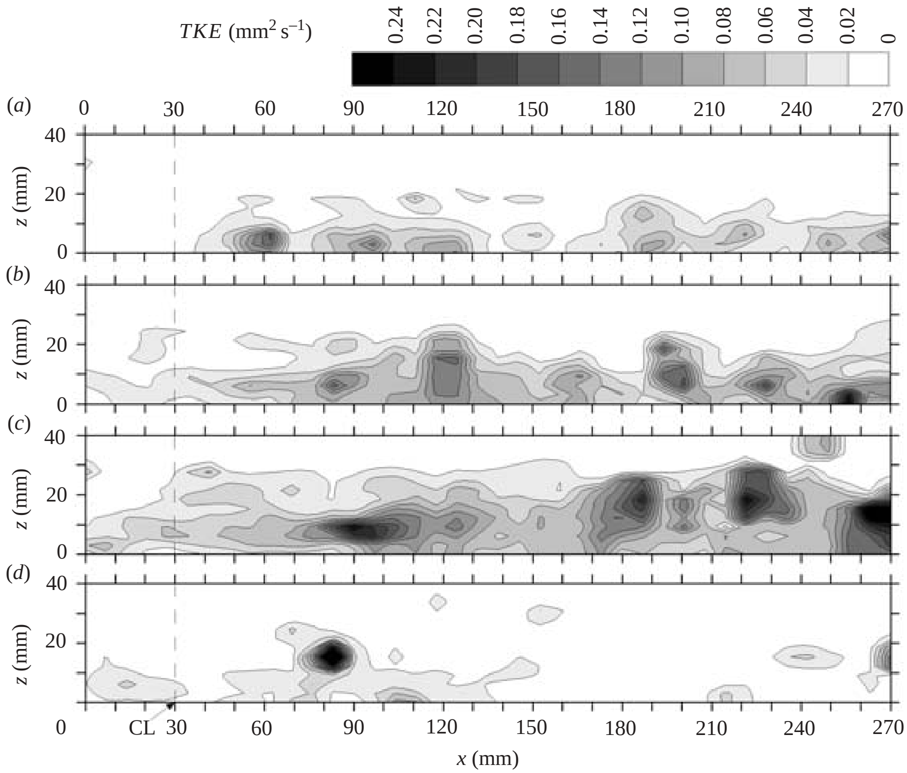

FIGURE 8. Turbulent kinetic energy (*TKE*, units mm^2 s^{-1}) taken during sequential phases of the thermal cycle (cf. figure 3): (*a*) cellular convection ($t' = 0.159$); (*b*) sea-breeze onset and front formation ($t' = 0.227$); (*c*) sea-breeze intrusion and front strengthening ($t' = 0.295$); (*d*) land-breeze ($t' = 0.864$).

velocity observed when the sea breeze is well established, see figure 6*d*) and by high *TKE* levels (figure 8*b*), responsible for intense mixing with the surrounding fluid.

Figures 5(*d*) and 5(*e*) show two velocity patterns taken during the period in which the temperature difference between sea and land (respectively, $t' = 0.295$ and $t' = 0.364$, cf. figure 4*a*) reached a maximum. At $t' = 0.295$, the sea-breeze front was located at $x \cong 260$ mm, whereas at $t' = 0.364$, it was outside the framed area. For both the pictures, the key feature is the formation of billows within the interfacial layer. In fact, we see the presence of vortex-like structures behind the head of the current, whose centres were located at $x \cong 100$ mm, $x \cong 190$ mm and $x \cong 225$ mm at $t' = 0.295$ (figure 5*d*), and at $x \cong 130$ mm and $x \cong 220$ mm at $t' = 0.364$ (figure 5*e*). The *TKE* contour plot taken at $t' = 0.295$ (figure 8*c*) reveals that these structures were characterized by high turbulent intensity. The combination of temperature and velocity differences between the two layers leads to the hypothesis that the formation of the above-mentioned vortex-like structures may be related to Kelvin–Helmholtz instability. In fact, formation and rolling up of billows within the interface between layers of different density moving relative to each other have been observed frequently in the atmosphere as well as in laboratory experiments (Simpson 1994). The hypothesis that the observed vortex-like structures can be characterized as Kelvin–Helmholtz billows is strengthened by comparing the present experiment with that performed by CMM. They found that during the sea-breeze phase, the value assumed by the time-averaged gradient Richardson number within the interfacial layer was typically around 0.25, i.e. the critical value obtained by Miles (1961) and Howard (1961) in their dynamic stability analysis. Such an occurrence, mainly observed in the wake of the front where high shear took place, paved the way for the formation of Kelvin–Helmholtz billows that grew and then broke down, enhancing the intensity of the turbulent wake behind the sea-breeze current head. Signatures of Kelvin–Helmholtz billows are evident from the analysis of figure 7(*c*), where the time history of both the velocity components taken at ($x = 180$ mm, $z = 19$ mm) are depicted. Figures 5(*d*) and 5(*e*) show that, for the period of the sea-breeze phase, the point under consideration was within the interfacial layer and, as figure 7(*c*) reveals, during the time interval $0.300 < t' < 0.430$, it experienced the passing of two vortical structures, as evidenced by the strong oscillations of U and W around zero. These oscillations propagated far from the interfacial layer and were responsible for the wavy perturbation detected close to the bottom (cf. the oscillation of W for $0.250 < t' < 0.430$ shown in figure 7*b*). This feature tended to become less important during the weakening phase of the sea-breeze current ($t' = 0.492$, figure 5*f*), where both the billowing and the wave perturbation were no longer present.

The transition period between sea- and land-breeze is shown in figure 5(*g*) ($t' = 0.659$). In the lower region ($z < 7$ mm), the fluid temperature was smaller than that of the initial temperature profile at the same height because of the cooling from the bottom surface (figure 4*b*). Also, the velocity approached zero within that layer while, owing to inertia, the sea breeze continued to flow above it. It can be observed that, in the neighbourhood of the CL, a land-breeze directed offshore was forming. Then, the land-breeze developed and attained its maximum intensity at approximately $t' = 0.864$ (figure 5*h*), in correspondence with the minimum temperature reached by the bottom surface (figure 4*b*).

The land-breeze can be recognized as being a typical stably stratified flow in which turbulence is only occasionally generated. In fact, the shear length scale $L_S = \sigma_w/(\mathrm{d}U/\mathrm{d}z)$ and the buoyancy length scale $L_b = \sigma_w/N$ of stratified turbulence are in the present case $L_S \cong 1.5$ mm and $L_b \cong 0.15$ mm, respectively (for typical values of $(\mathrm{d}U/\mathrm{d}z) = 0.047\,\mathrm{s}^{-1}$, $N = 0.75\,\mathrm{s}^{-1}$ and of the root mean square of the vertical velocity $\sigma_w = 0.07\,\mathrm{mm\,s}^{-1}$). Since $L_S/L_b = \overline{Ri_g}^{1/2} \gg 1$, turbulence is restricted to scales much smaller than those affected by shear, it is patchy in space and decays very rapidly. The *TKE* contour plot shown in figure 8(*d*) is a clear illustration of this feature. The spot located at $x \cong 80$ mm is related to the vortex-like structure visible in figure 5(*h*).

3.2. *POD analysis*

3.2.1. *POD eigenmodes and associated eigenvalues*

This subsection deals with the basic features of the POD eigenmodes and associated eigenvalues obtained by solving (2.2). The two point cross-correlation matrix $\boldsymbol{R}$ in (2.2) is evaluated by using the ensemble of the $M = t_C/\Delta t = 264$ time-averaged velocity fields calculated at the time instants $t'_i = i\Delta t'$, $i = 1, \ldots, M$, at each of the $N_N = 40 \times 30 = 1200$ grid nodes as described in the previous section (here $\Delta t' = \Delta t/t_C$). In particular, with $\Delta x = L/40$ and $\Delta z = H/30$ being the horizontal and the vertical length of a grid cell, N sets of eigenmodes $\{\Psi_k(x_l, z_h)\}_{l=1,40}^{h=1,30}$, $k = 1, \ldots, N$, and N eigenvalues $\{\lambda_k\}_{k=1,N}$, will be extracted. Here, $x_l = (l - 0.5)\Delta x$ and $z_h = (h - 0.5)\Delta z$ indicate the horizontal and the vertical grid node coordinate, respectively, and

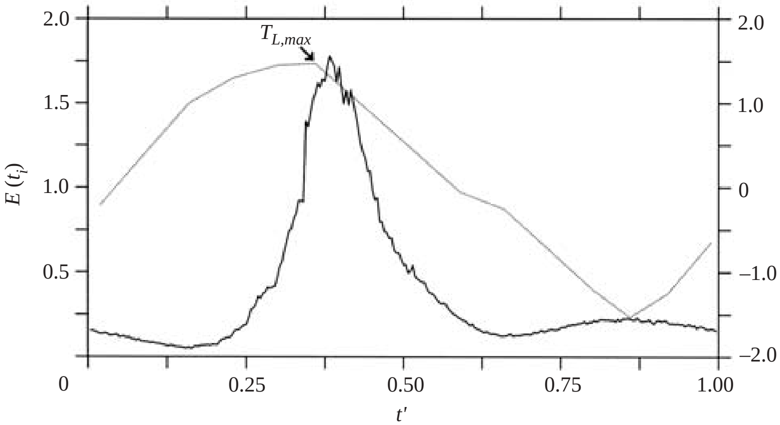

FIGURE 9. Time variation of the percentage rate of the turbulent kinetic energy $E(t_i')$ associated with the modes (solid line). The rate refers to energy retained by the total ensemble of modes at each time instant t_i' to that associated to the entire thermal cycle. The dotted line represents the actual thermal cycle.

$N = N_N \times n_c$, where $n_c = 2$ is the number of velocity components. It should be mentioned that the coherent structures related to the POD eigenmodes represent average shapes of the large-scale structures of the flow. In fact, as pointed out by Gordeyev & Thomas (2000), $\boldsymbol{R}$ gives a measure of the time-averaged large-scale correlation of the flow.

In order to quantify the energy content of the flow field, it is useful to evaluate the percentage rate $E(t_i')$ of the kinetic energy retained by the total ensemble of modes at each time instant t_i' to that of the flow field of the entire duration of the thermal cycle. Definition (2.5) gives:

$$E(t_i') = \frac{\sum_{k=1}^{N} \xi_k^2(t_i')}{\sum_{i=1}^{M} \sum_{k=1}^{N} \xi_k^2(t_i')} \times 100 \quad (i = 1, \ldots, M). \tag{3.1}$$

Figure 9 shows that $E(t_i')$ (solid line) reaches the absolute maximum during the sea-breeze phase ($t' \cong 0.380$), while a second maximum is attained during the land-breeze phase ($t' \cong 0.860$). The two minima correspond, respectively, to the phase of transition between land- and sea-breeze ($t' \cong 0.170$) and between sea- and land-breeze ($t' \cong 0.680$), which is when the horizontal velocities are at a minimum. The time of occurrence of the absolute maximum was delayed by ∼0.020 (∼30 min in the real world) with respect to that of the maximum land temperature (dotted line). Notice that this time delay did not take place for the second maximum recorded during the land-breeze phase. A possible reason may be the slower reduction of the land temperature during the cooling phase.

Information on the eigenmodes characteristics can be deduced by evaluating the amount of kinetic energy retained by each mode in comparison with the total kinetic energy of the flow field. A proper measure is the percentage relative energy $E_R(k)$, defined as the ratio between the energy retained by the mode number k and the

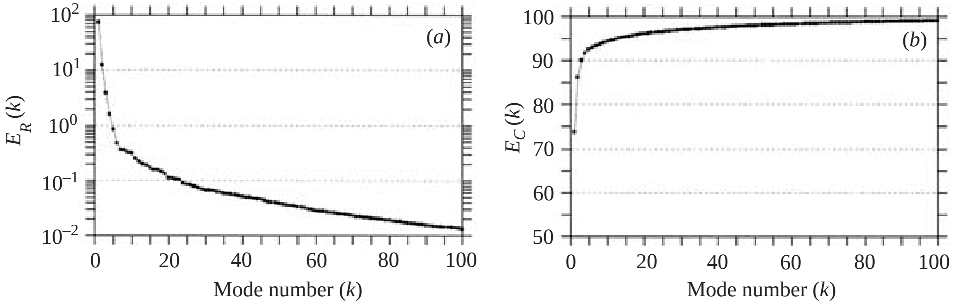

FIGURE 10. (*a*) Relative $E_R(k)$ and (*b*) cumulative $E_C(k)$ energies for the first 100 modes.

kinetic energy measured for the entire time duration of the thermal cycle:

$$E_R(k) = \frac{\sum_{i=1}^{M} \xi_k^2(t_i')}{\sum_{i=1}^{M}\sum_{k=1}^{N} \xi_k^2(t_i')} \times 100 \quad (k = 1, \ldots, N). \tag{3.2}$$

Additional information can be obtained by evaluating the cumulative energy $E_C(k)$, defined as the rate per cent between the amount of kinetic energy retained by the modes up to the kth mode and, likewise for $E_R(k)$, the kinetic energy measured for the whole time duration of the thermal cycle:

$$E_C(k) = \frac{\sum_{i=1}^{M}\sum_{j=1}^{k} \xi_j^2(t_i')}{\sum_{i=1}^{M}\sum_{k=1}^{N} \xi_k^2(t_i')} \times 100 \quad (k = 1, \ldots, N). \tag{3.3}$$

$E_R(k)$and $E_C(k)$, referring to the first 100 eigenvalues λ_k, $k = 1, \ldots, 100$, are shown in figures 10(*a*) and 10(*b*), respectively. Both figures show that the convergence was very rapid. In fact, the first mode contains approximately 73% of the total energy of the flow. Going to higher eigenvalues, the energy dropped rapidly. Notice that the first three modes combined contain more than 90% of the energy, whereas nearly 95% was associated with the first 12 modes. It is not surprising that such a large quantity of energy is retained by the first modes. In fact, POD theory states that among all linear decomposition methods, POD is optimal (in an energetic sense) in that for a given number of modes it retains the most kinetic energy possible (BHL). As a consequence, a low number (typically 4–5) of POD modes is sufficient for a good description of a flow field. Similar deductions were drawn by Gordeyev & Thomas (2000) in their investigation of a turbulent planar jet, and by Miozzi & Querzoli (1996) in their study of a quasi two-dimensional convective flow. Therefore, the notable result is that by making use of the modal decompositions in the eigenmodes expressed by (2.3), it is possible to reconstruct the original velocity field by means of a small number of POD modes. However, this statement must be treated with caution, since, as will be shown later, the number of modes needed for a good quality reconstruction of the flow field is strongly dependent on the phase of the thermal cycle.

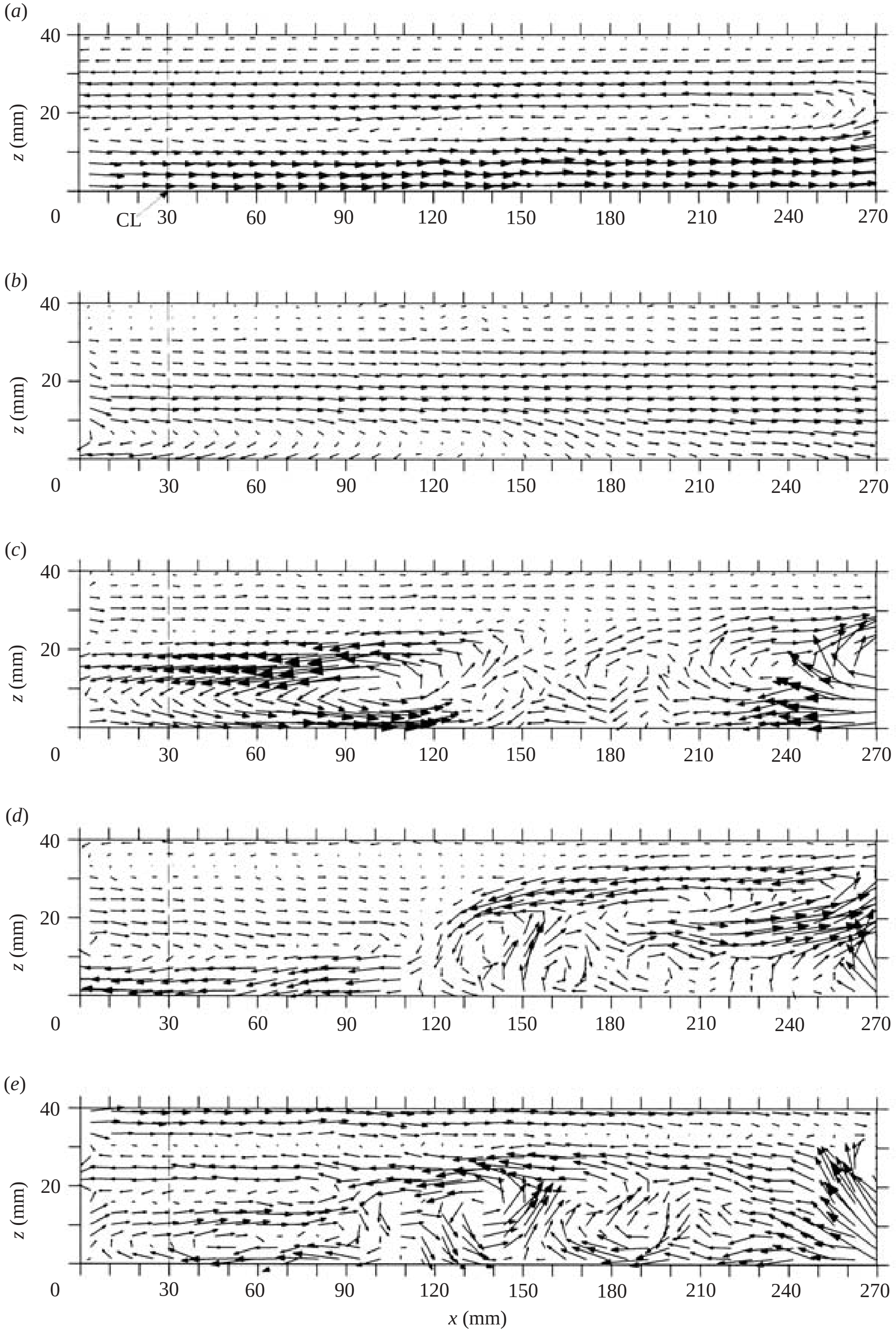

FIGURE 11. POD first five modes: (a) ψ_1; (b) ψ_2; (c) ψ_3; (d) ψ_4; (e) ψ_5.

Figure 11 depicts the vector representations of the first five modes $\{\Psi_k(x_l, z_h)\}_{l=1,40}^{h=1,30}$, $k = 1, \ldots, 5$, obtained at each of the N_N grid nodes; the time behaviour of the associated modal amplitudes $\xi_k(t_i')$, $k = 1, \ldots, 5$, $i = 1, \ldots, M$ are presented in figure 12.

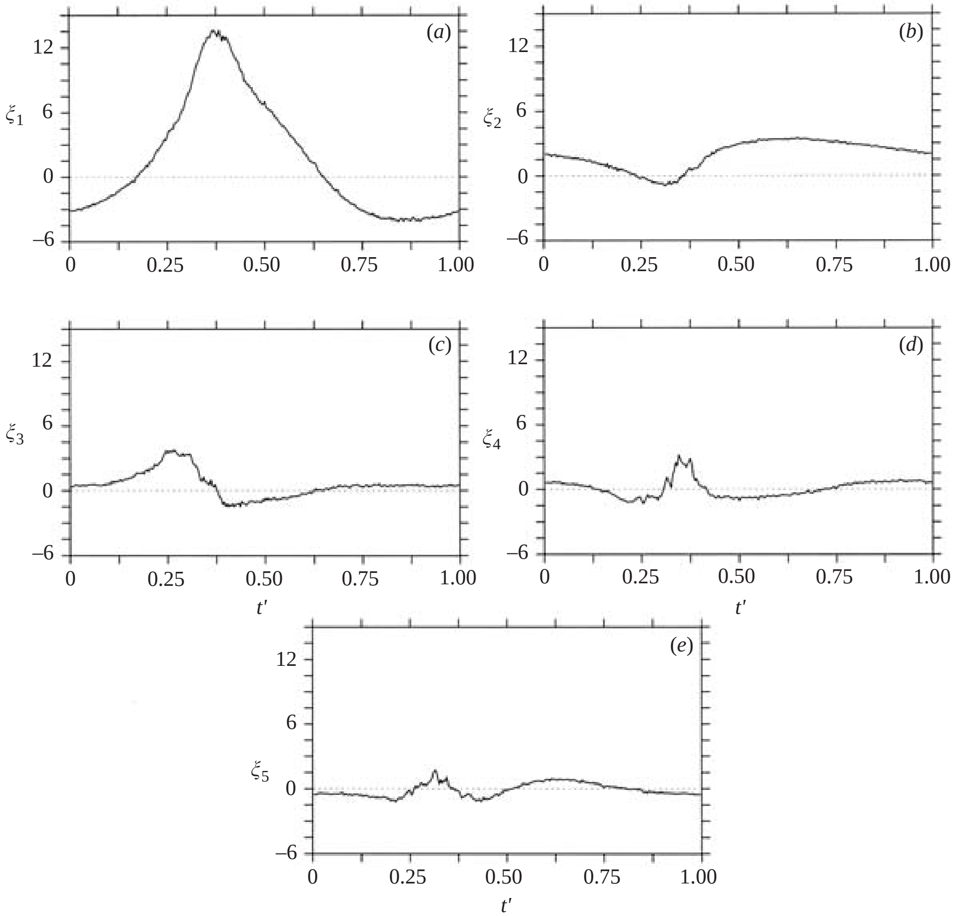

FIGURE 12. Time series of the modal amplitude associated with the modes shown in figure 11: (*a*) ξ_1; (*b*) ξ_2; (*c*) ξ_3; (*d*) ξ_4; (*e*) ξ_5.

The first, most energetic, mode ($k=1$) should correspond to the mean flow and, as illustrated in figure 11(*a*), it was strictly related to the phases of land and sea breeze (cf. figure 5*a* and 5*e*, respectively). We see from the figure that the first modal amplitude ξ_1 (figure 12*a*) peaked at $t' \cong 0.380$, i.e. during the maximum intensity of the sea breeze (figure 5*e*). Also, ξ_1 was positive during the sea-breeze phase ($0.170 < t' < 0.630$) and negative during the land-breeze phase. In the latter case, the (negative) maximum recorded at $t' \cong 0.852$ was about a third of the (positive) maximum attained at $t' \cong 0.380$, as a result of the greater kinetic energy associated with the sea-breeze with respect to the land-breeze circulation.

Comparing the pattern of the second mode Ψ_2 (figure 11*b*) and the flow field taken at $t'=0.659$ (cf. figure 5*g*) reveals that Ψ_2 was related to the phase of transition between the sea and land breezes. This hypothesis is strengthened by analysis of the time behaviour of the associated modal amplitude ξ_2 (figure 12*b*), characterized by a peak at $t' \cong 0.65$. Notice that the other modal amplitudes associated with the ξ_2 maximum were approximately zero.

The third mode (figure 11*c*) characterizes the phase of penetration of the sea-breeze current (figure 5*c*). The vortex-like structures at $x > 150\,\text{mm}$ were related to

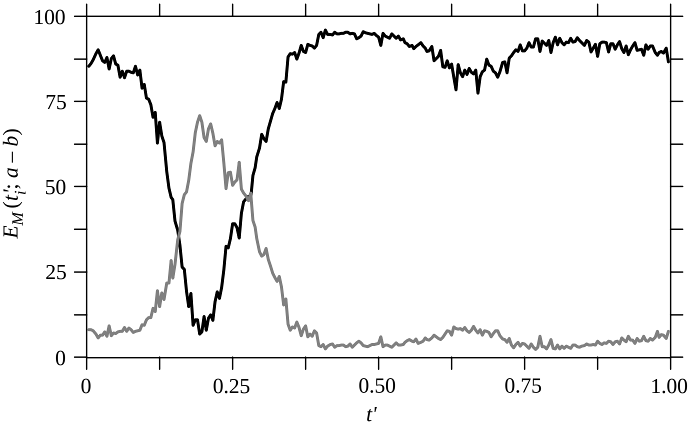

FIGURE 13. Time series of the percentage rate $E_M(t_i'; a-b)$ of the energy contained in the modes for $a=1$, $b=2$ (solid line) and for $a=3$, $b=12$ (grey line).

those recognized during the phase of sea-breeze intrusion and front strengthening (cf. figure 5*d*). For $k=4$ and $k=5$ (respectively, figures 11*d* and 11*e*) the predominant structures were associated mainly to convective activities. In fact, their modal amplitudes (figure 12*d* and 12*e*) were always nearly zero, with the exception of the time interval of the maximum bottom surface temperature (figure 4). For $k \geqslant 6$, the eigenmodes and associated eigenvalues (not shown) had trends similar to those observed for $k=5$, suggesting that they were all related to the cellular convection phase. However, the curves of the modal amplitude for $k \geqslant 6$ reveal that the importance of such structures tended to be negligible as the mode number increased.

An alternative analysis of the relative importance of different modes at different time instants is presented in figure 13, where the curves show the ratio:

$$E_M(t_i'; a-b) = \frac{\sum_{k=a}^{b} \xi_k^2(t_i')}{\sum_{k=1}^{N} \xi_k^2(t_i')} \times 100 \quad (i=1, \dots, M), \tag{3.4}$$

for $a=1$ and $b=2$ (solid line) and $a=3$ and $b=20$ (dashed line) are drawn. It is apparent that the first two modes were always prominent except for the time interval $0.160 < t' < 0.270$, i.e. when convective cells reached their maximum activity.

3.2.2. *Reconstruction of the mean velocity fields via POD modes*

In this subsection, the restored mean velocity fields obtained by the modal decomposition in the eigenmodes expressed by (2.3) are compared to the original (experimental) ensemble of velocity fields. As mentioned earlier, the effectiveness of this approach is based on the assumption that the POD decomposition is optimal for reconstructing any signal $\boldsymbol{u}(\boldsymbol{x}, t)$ and that it is possible to reconstruct the original vector fields by means of a small number of POD modes. The question then arises as to whether or not the number of POD modes needed to restore the shape of the averaged velocity fields depends on the characteristics of the flow (i.e. on the phase of the thermal cycle). A quantitative estimate of the differences between the original and the reconstructed velocity fields can be given evaluating the percentage, non-dimensional mean square error $\varepsilon(t_i', k)$, defined as:

$$\varepsilon(t_i', k) = \frac{\left\langle \left[\left(\sum_{j=1}^{k} \xi_j(t_i') \psi_j(\boldsymbol{x}) \right) - \boldsymbol{u}(\boldsymbol{x}, t_i') \right]^2 \right\rangle}{\langle \boldsymbol{u}(\boldsymbol{x}, t_i')^2 \rangle} \times 100 \quad (i = 1, \dots, M), \qquad (3.5)$$

and its time average $\varepsilon_t(k)$. Figure 14(*b*), where $\varepsilon_t(k)$ is depicted for $k = 1, \dots, 200$, illustrates that 10 modes were sufficient to reconstruct the flow field with an average error of 6% and that by using 40 modes the error dropped below 2.5%. However, owing to the non-stationarity of the flow field, $\varepsilon(t_i', k)$ depended strongly upon the phase of the thermal cycle at which the modal reconstruction was performed. In fact, figure 14(*a*) suggests that four well-defined regions, i.e. land- and sea-breeze regimes and the two transition periods in between, characterized the $\varepsilon(t_i', k)$ behaviour. In particular, $\varepsilon(t_i', k)$ attained a maximum within the time interval $0.417 < t' < 0.455$, i.e. during the sea-breeze phase, when both thermal convection and a gravity current occurred. A second maximum took place during the maximum strength of the land breeze ($t' \cong 0$). We notice the strong oscillation of $\varepsilon(t_i', k)$ during the convective phase, when large convective cells slowly followed one another above the land surface. This behaviour can be explained by the basic property of the POD, namely, the eigenmodes of the correlation matrix $\boldsymbol{R}$ are the 'most correlated' in an average sense, but not at a generic time instant. Figure 14(*a*) also shows that, during the sea-breeze phase, ∼40 modes were required to obtain an error of ∼20%, and that the number of modes increased to ∼140 in order to obtain an error of ∼5%. On the other hand, during the phase of cellular convection, ∼40 modes were sufficient to ensure that the error was not greater than 5%.

An example of the modal reconstruction is presented in figure 15, where the 'original' velocity field taken at $t' = 0.159$ (corresponding to the phase of cellular convection, cf. figure 5*b*) is rebuilt for $k = 1 - 5$, $k = 1 - 10$, $k = 1 - 20$ and $k = 1 - 50$ (figures 15*a*–15*d*). Notice that as k increases, so does the overall resemblance between the reconstructed and the original field. During the transition phase between sea and land breeze, the number of modes necessary to reconstruct the velocity field decreased dramatically (figure 16*a*,*b*). Here, for $k = 1 - 10$ (figure 16*b*), the resemblance with the original field ($t' = 0.659$, cf. figure 5*g*) is already apparent. This result is consistent with the discussion of figure 13(*a*). Note that, in both cases, a further increase in the number of modes decreases the differences between reconstructed and original fields.

Finally, it is worth noting that the POD approach used in this section, known in the literature as classical POD (Cordier & Bergmann 2002), is one of the two different existing POD approaches, i.e. the classical POD and the snapshot POD (Sirovich 1987). The former has proved to be well suited when the data are issued from experimental techniques, and the latter when the data are taken from numerical simulations (Cordier & Bergmann 2002). We repeated the analysis illustrated above by using the snapshot POD and, not surprisingly, we found that the eigenfunctions exhibited characteristics analogous to those carried out with the classical POD approach.

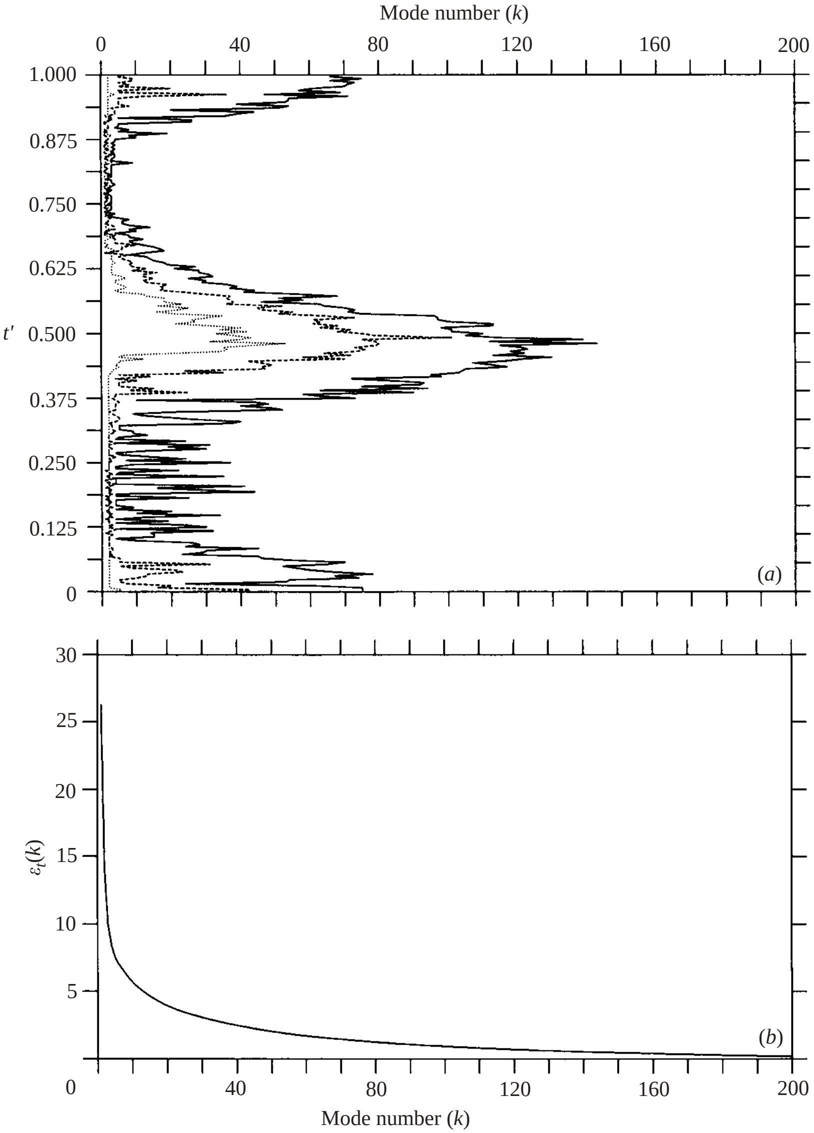

FIGURE 14. (*a*) Percentage error $\varepsilon(t'_i, k)$ as a function of the number of modes used to rebuild the instantaneous flow fields. Isolevels at 5% (solid line), 10% (long dashes) and 20% (short dashes) are shown; (*b*) time-averaged percentage error $\varepsilon_t(k)$.

4. Summary and discussion

The ‘pure’ LSB observable in the atmosphere in the proximity of shorelines was produced in a laboratory experiment. A temperature controlled water tank was used to reproduce the diurnal cycle of incident solar radiation and PTV has been applied to evaluate the velocity field in a vertical section at the centreline of the tank perpendicular to the coastline. A rack of thermocouples allowed acquisition of a vertical profile of the fluid temperature in the proximity of the shoreline and further inland. The experiment highlighted the dynamics of the various phenomena involved throughout the entire cycle of warming and cooling of the land side. In particular,

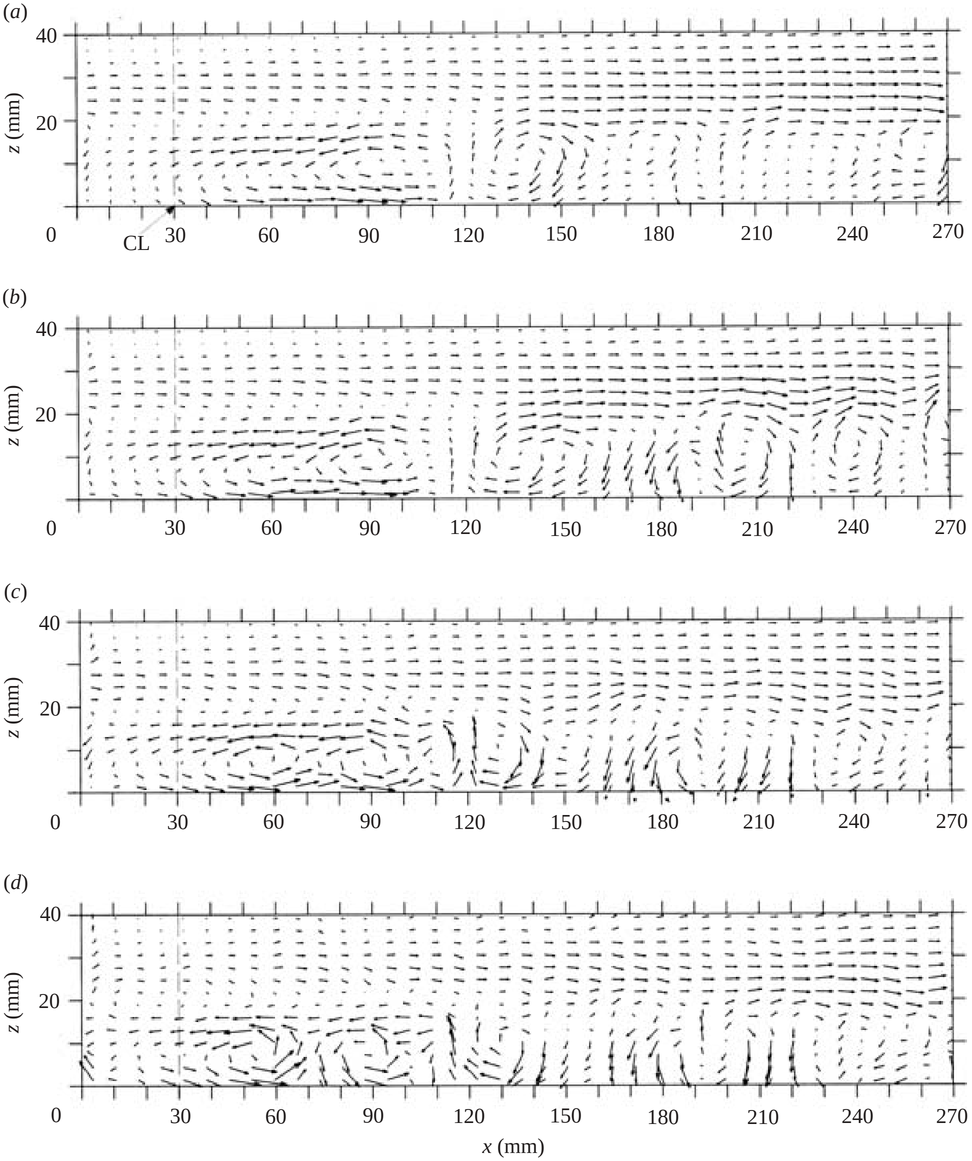

FIGURE 15. Reconstructed velocity fields at $t' = 0.159$ as a function of the number of modes: (a) 5 modes; (b) 10 modes; (c) 20 modes; (d) 50 modes. The measured field is shown in figure 5(b).

the overall LSB circulation together with the genesis and inland penetration of the front at the leading edge of the sea-breeze flow were described. The salient findings of the present study can be summarized as follows:

(i) Rayleigh–Bénard cellular convection was detected during the first phase of warming, as is the manner by which the sea breeze produced a strong decrease of the kinetic energy inland. Furthermore, vortex-like structures, characterized by relatively high turbulent kinetic energy levels, were observed in the wake of the sea-breeze front and, based on previous experiments conducted by CMM, they might be associated with Kelvin–Helmholtz billowing.

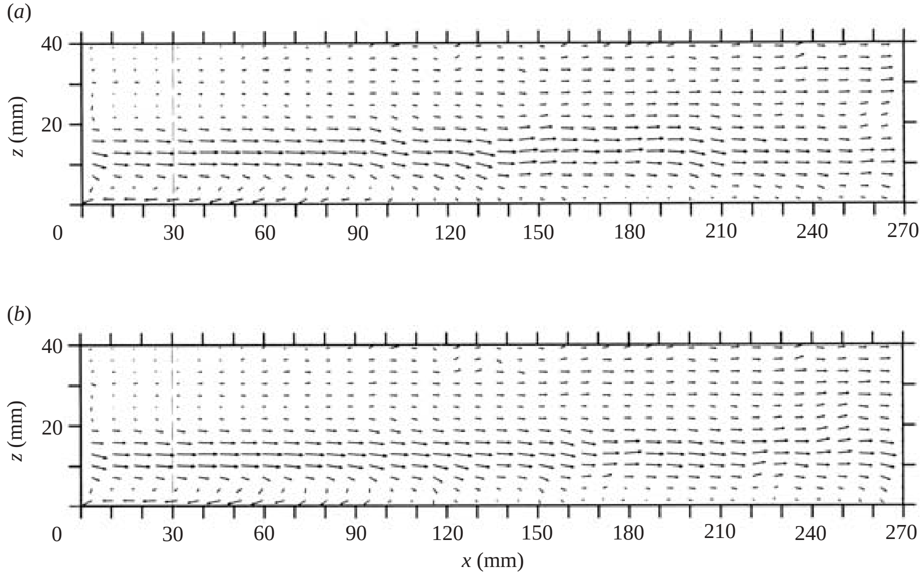

FIGURE 16. Reconstructed velocity fields at $t' = 0.659$ as a function of the number of modes: (*a*) 5 modes; (*b*) 10 modes. The measured field is shown in figure 5(*g*).

(ii) Characteristics of the vortical large-scale structures in the velocity field were revealed using the POD technique. To our knowledge, this is the first time that POD has been applied to two-dimensional flow fields obtained by experimental simulations, in particular, when varying with time thermal forcing is present. The analysis showed that the convergence of the POD modes was very rapid. The first mode retained approximately 73% of the kinetic energy, the first three modes captured nearly 90% whereas 95% of the energy was contained in the first twelve modes.

(iii) It was shown that the first, most energetic, two modes were related to the phases of sea and land breeze, according to the basic concept that the POD is well suited to recognize the most energetic structures of the flow field. The other modes were mainly associated with the convective activity that developed inland during the first phase of warming. It should be noted that the rapid modal convergence of the POD technique paves the way for the use of the Galerkin projection of the equations of motion onto the first modes as an empirical basis well suited to capture the large-scale dynamics of the flow (Aubry *et al.* 1988; Ukeiley & Glauser 1995; Ukeiley *et al.* 2001). The truncated modes can be modelled as dissipation that affects the most energetic scales.

(iv) The reconstruction of the instantaneous velocity fields via the modal decompositions in the eigenmodes showed that the number of modes necessary for a good approximation of the 'original' (experimental) flow patterns strongly depended on the phase of the cycle. Although the time-averaged error had a steep drop as the number of modes involved in the reconstruction increased, the value of the instantaneous error showed a well-defined temporal behaviour with a maximum attained at the sea-breeze phase as well as rapid oscillations during the cellular convection. This is a consequence of the eigenmodes of the correlation matrix being the most correlated structures in an average sense, but not at a generic time instant. This should be kept in mind whenever the modes are used as bases of dynamical systems.

A question arises as to whether or not the model results are in dynamic similarity with the full-scale phenomena. The similarity variables to be matched between the full-scale and the laboratory simulation can be found by invoking the governing equations of motion and thermodynamic energy. Following Ueda (1983), it is possible in the framework of the linear theory to determine the dimensionless external parameters and their effects on the scales of the LSB circulation. In particular, the following dimensionless variables (with asterisks) are defined:

$$\left.\begin{array}{l} t^* = t\omega, \quad (x^*, y^*, z^*) = (x, y, z)/L, \quad b^* = b/b_{max}, \\ (U^*, V^*, W^*) = (\omega/b_{max})(U, V, W), \quad p^* = p/(b_{max}L), \end{array}\right\} \tag{4.1}$$

where $\omega = (2\pi)/t_C$ indicates the angular velocity of temperature variation (i.e. the angular velocity of the earth's rotation), $L = (\nu/\omega)^{1/2}$ the length scale associated with the momentum diffusion (ν is the kinematic viscosity), (U,V,W) the velocity components in the (x, y, z)-axis, respectively, b_{max} the value of the maximum difference between the sea and land surfaces of the buoyancy term $b = g\alpha\theta$ (here, θ is the deviation of the potential temperature from the basic state Θ) and p the static pressure. In this context, L, ω^{-1} and b_{max} represent, respectively, the scales of length, time and buoyancy.

For a two-dimensional LSB in the case of flat terrain and in the absence of geostrophic wind, using the Boussinesq approximation and assuming a constant eddy diffusivity for heat and momentum (ν and κ), Ueda (1983) obtained a linearized set of non-dimensional equations for the deviations from the basic flow field in which the key parameters were the Grashof number $Gr = g\alpha\Gamma L^4/\nu^2$ and the Prandtl number $Pr = \nu/\kappa$ (here $\Gamma = \mathrm{d}\Theta/\mathrm{d}z$ is the basic lapse rate). Ueda (1983) analysed the dependence of Gr and Pr on the strength and on both the horizontal and vertical scales of the LSB and found that they can be expressed in the form:

$$U_{ref} \propto Gr^{-1/2}Pr^{-2/3}, \quad \mathrm{x}_{ref} \propto Gr^{0.387}, \quad \mathrm{z}_{ref} \propto Pr^{-1/4}, \tag{4.2}$$

around a standard state of the atmosphere. U_{ref} represents the maximum horizontal velocity of the breeze current while x_{ref} and z_{ref} are defined as the distance from the CL where U is greater than 50% of the value assumed at x_{CL} and the depth of the sea breeze, respectively. Ueda also found that the relations (4.2) hold true over a wide range of variation of Gr and Pr (more than two orders of magnitude). This suggests that the following non-dimensional variables:

$$U^+ = U^* Gr^{1/2} Pr^{2/3}, \quad \mathrm{x}^+ \propto x^* Gr^{-0.387}, \quad \mathrm{z}^+ \propto z^* Pr^{1/4}, \tag{4.3}$$

are universal similarity parameters for the LSB circulation. They are useful for comparing field observations performed under different conditions, as well as laboratory models with field observations.

Table 1 reports the values of the variables related to the present experiment and those observed in a field campaign performed in the proximity of the shoreline near Rome, Italy (Leuzzi & Monti 1997), complemented by numerical results obtained by a numerical mesoscale model applied to the same region (Monti & Leuzzi 1999). From the analysis of table 2, where the non-dimensional parameters (4.3) for the two cases are reported, it can be observed that such quantities are in reasonable agreement, even though non-negligible discrepancies in the velocity scale U^+ and the horizontal scale x^+ are present. It should be noted that the values for the field observation considered here were taken for a case in which geostrophic winds were present ($\sim 3\,\mathrm{m\,s^{-1}}$) rather than the 'pure' LSB simulated in the laboratory. Table 2 also reports the non-dimensional parameters (4.3) referred to in the data set of

	ω (rad s^{-1})	ν (m^2 s^{-1})	α (°C^{-1})	Γ (°C m^{-1})	θ_{max} (°C)	L (m)	b_{max} (m s^2)	Gr	Pr
Present experiment	2.37×10^{-3}	1×10^{-6}	2.60×10^{-4}	1×10^{2}	1.5	0.021	0.0038	49 604	6.3
Field observations	7.27×10^{-5}	5×10^{0}	3.48×10^{-3}	5×10^{-3}	6	262	0.20	32 171	0.72

TABLE 1. Main variables of the present experiment and field data (Leuzzi & Monti 1997).

	U (m s^{-1})	U^*	U^+	x (m)	x^*	x^+	z (m)	z^*	z^+
Present experiment	0.001	0.00062	**0.47**	0.6	38.1	**0.61**	0.015	0.71	**1.13**
Field observations	5	0.00181	**0.26**	20000	152.67	**1.37**	300	1.15	**1.06**
CMM			**0.16**			**0.66**			**1.55**

TABLE 2. Comparison among non-dimensional parameters (4.3) calculated for the present experiment, the CMM experiment and for the field data of Leuzzi & Monti (1997).

CMM, in which the amplitude of the thermal cycle and the vertical gradient of the ambient temperature were set to $T_C = 2\,°\mathrm{C}$ and $\partial T_a/\partial z = 0.05\,°\mathrm{C\,mm}^{-1}$, respectively. It is apparent that there is a discrepancy for the values of the velocity scale U^+. This disagreement is probably due to the small Reynolds number $Re = UL/\nu$ of both the experiments ($Re \cong 15$ for the present data set and $Re \cong 10$ for the CMM data set), mainly due to the limitation of the tank size, which gives rise to a dependency of the velocity field on Re. In fact, the laboratory experiments performed by Keulegan (1957) showed that the velocity of a gravity current head does not depend on Re only for $Re > 1000$, a value impossible to attain with our experimental set-up.

Another limitation of the experiment is related to the small Rayleigh number achieved during the heating phase, $Ra \sim 3 \times 10^3$, i.e. several orders of magnitude less than those typically observed in the atmosphere. This may explain the strong lessening in TKE levels measured after the passage of the sea-breeze front, an event that does not happen in nature. However, the Ra value of the laboratory experiment was large enough to make the flow unstable, i.e. to cause cellular convection over land in the morning hours.

This work was supported by funds from the MIUR. The authors are grateful to Professor P. F. Linden for his useful comments and suggestions and Professor G. Querzoli for discussions concerning the PTV technique. They also wish to thank Dr C. Adduce, Dr F. Ciotti, Dr M. Marchetti and Mr F. Sammartino for their help in collecting the data.

REFERENCES

AUBRY, N., HOLMES, P., LUMLEY, J. L. & STONE, E. 1988 The dynamics of coherent structures in the wall region of the turbulent shear layer. *J. Fluid Mech.* **192**, 115–175.

BERKOOZ, G., HOLMES, P. & LUMLEY, J. L. 1993 The proper orthogonal decomposition in the analysis of turbulent flows. *Annu. Rev. Fluid Mech.* **25**, 539–575 (referred to herein as BHL).

CENEDESE, A., MIOZZI, M. & MONTI, P. 2000 A laboratory investigation of land and sea breeze regimes. *Exps. Fluids* **29**, 291–299 (referred to herein as CMM).

Cenedese, A. & Querzoli, G. 1994 A laboratory model of turbulent convection in the atmospheric boundary layer. *Atmos. Environ.* **28**, 1901–1913.

Chiba, O. 1993 The turbulent characteristics in the lowest part of the sea breeze front in the atmospheric surface layer. *Boundary Layer Met.* **65**, 181–195.

Cordier, L. & Bergmann, M. 2002 Proper orthogonal decomposition: an overview. *Lecture Series 2002–2004 on Post processing of Experimental and Numerical Data* (ed. P. Millian & M. L. Riethmuller), pp. 1–45. Von Kármán Institute for Fluid Dynamics, Rhode Saint Genèse, Belgium.

Deardorff, J. W. & Willis, G. E. 1985 Further results from a laboratory model of the convective planetary boundary layer. *Boundary Layer Met.* **32**, 205–236.

Delville, J., Ukeiley, L. Cordier, L., Bonnet, J. P. & Glauser, M. 1999 Examination of large scale structures in a plane mixing layer. Part 1. Proper orthogonal decomposition. *J. Fluid Mech.* **391**, 91–122.

Fisher, M., Wiegel, M., Herberg, T. & Heiderich, G. 1996 Flow field decomposition applied to experimental data obtained for a transitional boundary layer. *Appl. Sci. Res.* **56**, 103–112.

Glauser, M. N. & George, W. K. 1989 An orthogonal decomposition of the axisymmetric jet mixing layer. In *Turbulent Shear Flows 6* (ed. Y. C. Andre *et al.*). Springer.

Gordeyev, S. V. & Thomas, F. O. 2000 Coherent structure in the turbulent planar jet. Part 1. Extraction of proper orthogonal decomposition eigenmodes and their self-similarity. *J. Fluid Mech.* **414**, 145–194.

Helmis, C. G., Asimakopoulos, D. N., Deligiorgi, D. G. & Lalas, D. P. 1987 Observation of sea-breeze front near the shore-lines. *Boundary Layer Met.* **38**, 395–410.

Holmes, P., Lumley, J. L. & Berkooz, G. 1996 *Turbulence, Coherent Structures and Symmetry.* Cambridge University Press.

Howard, L. N. 1961 Note on a paper of John W. Miles. *J. Fluid Mech.* **13**, 258–260.

Keulegan, G. H. 1957 An experimental study of the motion of the salt water from locks into fresh water channels. *US Natl Bur. Stand. Rep.* 5168.

Kobayasi, T., Sasaki, T. & Osanay, T. 1937 Theoretical and experimental studies of convectional circulation and its relations to land and sea-breezes. *Rep. Aeronaut. Res. Inst. Tokyo* **12**, 67 pp.

Koschmieder, E. L. 1993 *Bénard Cells and Taylor Vortices.* Cambridge University Press.

Koschmieder, H. 1936 Danziger seewindstudien, I. *Dan Met. Forsch.* **8**, 45 pp.

Leuzzi, G. & Monti, P. 1997 Breeze analysis by mast and sodar measurements. *Il Nuovo Cimento* **20 C**, 343–359.

Linden, P. F. & Simpson, J. E. 1986 Gravity-driven flows in a turbulent fluid. *J. Fluid Mech.* **172**, 481–497.

Lumley J. L. 1967 The structure of inhomogeneous turbulent flows. In *Proc. Intl Colloq. on the Fine Scale Structure of the Atmosphere and its Influence on Radio Wave Propagation* (ed. A. M. Yaglom & V. I. Tatarsky), pp. 166–178. Dokl. Akad. Nauk SSSR, Moskow, Nauka.

Lumley, J. L. 1981 Coherent structures in turbulence. In *Transition and Turbulence* (ed. R. E. Meyer), pp. 215–241. Academic.

Miles, J. W. 1961 On the stability of heterogeneous shear flows. *J. Fluid Mech.* **10**, 496–508.

Miozzi, M. & Querzoli, G. 1996 PTV and POD analysis of the instability in a quasi two-dimensional convective flow. *Appl. Sci. Res.* **56**, 221–242.

Mitsumoto, S., Ueda, H. & Ozoe, H. 1983 A laboratory experiment on the dynamics of the land and sea breeze. *J. Atmos. Sci.* **40**, 1228–1240.

Moeng, C. H. 1984 Eddies in the atmosphere. *Annu. Rep., Fiscal Year 1983, National Center for Atmospheric Research* NCAR/AR-83, pp. 57–58.

Monti, P. & Leuzzi, G. 1999 Numerical investigation of flow and dispersion in presence of urban heat island. *Proc. of the 4th Intl Cong. on Energy, Environment and Technological Innovation,* September 20–24, Rome, Italy.

Pardyjak, E. R., Monti, P. & Fernando, H. J. S. 2002 Flux Richardson number measurements in stable atmospheric shear flows. *J. Fluid Mech.* **459**, 307–316.

Raynor, G. S., Hayes, J. V. & Odgen, E. C. 1974 Mesoscale transport and dispersion of airborne pollens. *J. Appl. Met.* **13**, 87–95.

SHA, W., KAWAMURA, T. & UEDA, H. 1991 A numerical study on sea/land breezes as a gravity current: Kelvin–Helmholtz billows and inland penetration of the sea-breeze front. *J. Atmos. Sci.* **48**, 1649–1665.

SIMPSON, J. E. 1994 *Sea Breeze and Local Winds*. Cambridge University Press.

SIMPSON, J. E. & BRITTER, R. E. 1980 A laboratory model of an atmospheric mesofront. *Q. J. R. Met. Soc.* **106**, 485–500.

SIMPSON, J. E. & LINDEN, P. F. 1989 Frontogenesis in a fluid with horizontal density gradients. *J. Fluid Mech.* **202**, 1–16.

SIROVICH, L. 1987 Turbulence and the dynamics of coherent structures. Part I: coherent structures. *Q. Appl. Maths* **45**, 561–571.

STULL, R. B. 1988 *An Introduction to Boundary Layer Meteorology*. Kluwer.

UEDA, H. 1983 Effects of the external parameters on the flow field in the coastal region. A linear model. *J. Clim. Appl. Met.* **22**, 312–321.

UKEILEY, L., CORDIER, L., MANCEAU, R., DELVILLE, J., GLAUSER, M. & BONNET, J. P. 2001 Examination of large-scale structures in a turbulent plane mixing layer. Part 2. Dynamical system model. *J. Fluid Mech.* **441**, 67–108.

UKEILEY, L. & GLAUSER, M. 1995 Dynamics of large-scale structures in a plane turbulent mixing layer. *Rep.* MAE-311. Department of Mechanical and Aeronautical Engineering, Clarkson University.

WALSH, J. E. 1974 Sea breeze theory and applications. *J. Atmos. Sci.* **31**, 2012–2026.